

Refining perovskite structures to pair distribution function data using collective Glazer modes as a basis

Sandra Helen Skjærvø,^a Martin A. Karlsen,^b Riccardo Comin^c and Simon J. L. Billinge^{a,d,*}

Received 16 February 2022

Accepted 28 July 2022

Edited by A. Fitch, ESRF, France

Keywords: inorganic materials; materials modelling; perovskites; structure refinement; pair distribution functions; octahedral rotations; geometric modelling.

Supporting information: this article has supporting information at www.iucrj.org

^aDepartment of Applied Physics and Applied Mathematics, Columbia University, New York, NY 10027, USA,

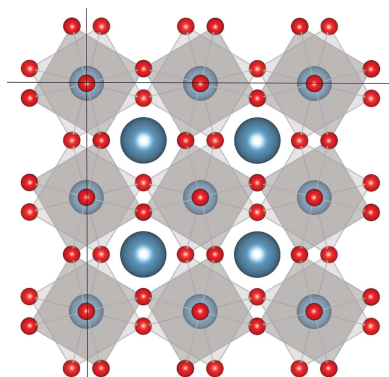
^bDepartment of Physics, Chemistry and Pharmacy, University of Southern Denmark, 5230 Odense M, Denmark, ^cPhysics Department, Massachusetts Institute of Technology, Cambridge, MA 02139, USA, and ^dCondensed Matter Physics and Materials Science Department, Brookhaven National Laboratory, Upton, NY 11973, USA. *Correspondence e-mail: sb2896@columbia.edu

Structural modelling of octahedral tilts in perovskites is typically carried out using the symmetry constraints of the resulting space group. In most cases, this introduces more degrees of freedom than those strictly necessary to describe only the octahedral tilts. It can therefore be a challenge to disentangle the octahedral tilts from other structural distortions such as cation displacements and octahedral distortions. This paper reports the development of constraints for modelling pure octahedral tilts and implementation of the constraints in *diffpy-CMI*, a powerful package to analyse pair distribution function (PDF) data. The model in the program allows features in the PDF that come from rigid tilts to be separated from non-rigid relaxations, providing an intuitive picture of the tilting. The model has many fewer refinable variables than the unconstrained space group fits and provides robust and stable refinements of the tilt components. It further demonstrates the use of the model on the canonical tilted perovskite CaTiO_3 which has the known Glazer tilt system $\alpha^+\beta^-\beta^-$. The Glazer model fits comparably to the corresponding space-group model *Pnma* below $r = 14 \text{ \AA}$ and becomes progressively worse than the space-group model at higher r due to non-rigid distortions in the real material.

1. Introduction

Structural distortions in materials, such as those occurring during displacive structural phase transitions, often involve collective displacements of groups of atoms (Dove, 1997). For example, in the perovskites, a material class with the nominal stoichiometry ABX_3 (Fig. 1), collective distortions are known to cause a host of structural phase transitions that lower the symmetry of the cubic parent structure (Müller *et al.*, 1968; Salje, 1990; Goodenough, 1955; Kwei *et al.*, 1993, 1995). Perovskites have a host of interesting and practical properties and are highly prized as ferroelectrics (Bhalla *et al.*, 2000; Benedek & Fennie, 2013), and even as photoactive materials in emerging photovoltaic technologies (Paillard *et al.*, 2016). It is critical to be able to model and characterize the nature of the distortions and their origin to properly understand and engineer these interesting properties. Because of the collective motions of the atoms in the distortions, a challenge is to come up with data-modeling approaches that capture these collective atomic displacements in a small number of variables.

Distortions away from the cubic archetype can involve deformations of the octahedra, displacements of the *B* cations inside the octahedra and tilting of the octahedra. The first two are typically caused by electronic instabilities, while the latter



Published under a CC BY 4.0 licence

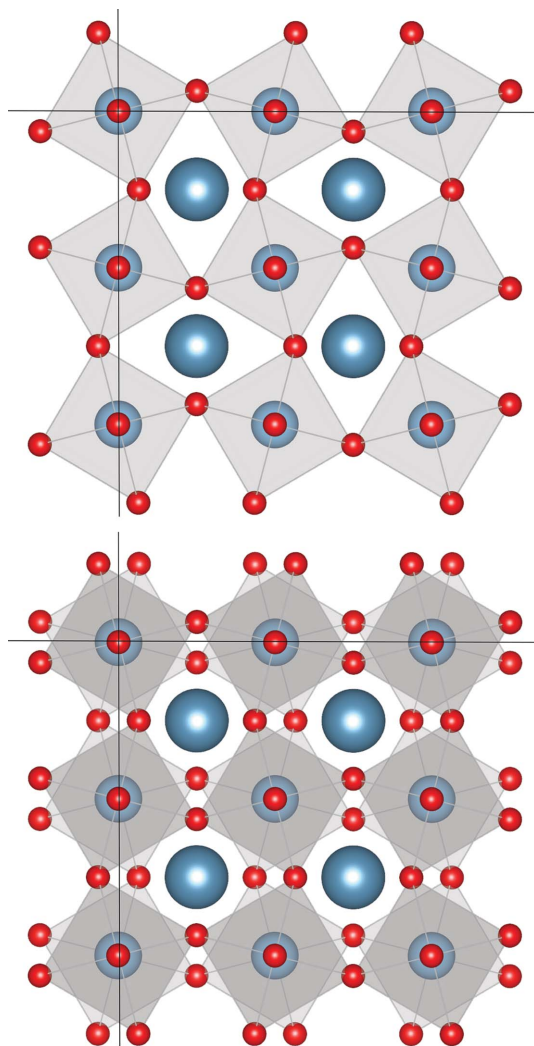


Figure 1
Illustration of in-phase and out-of-phase tilt systems as viewed down the tilt axis. The tilt systems shown here are $\alpha^0\alpha^0\gamma^+$ (top) and $\alpha^0\alpha^0\gamma^-$ (bottom).

is due to the relative sizes of the cations. For perovskites with smaller A cations, the octahedra tilt to compress the structure around them, essentially improving the bonding for the A cation. This geometric effect is conveniently captured by the Goldschmidt tolerance factor (Goldschmidt, 1926),

$$t = \frac{r_A + r_X}{\sqrt{2}(r_B + r_X)}, \quad (1)$$

where r is an ionic radius and subscripts A , B and X denote the ion type. For $t = 1$, the perovskite crystallizes in the high-symmetry cubic structure, whereas octahedral tilting is expected for a $t < 1$ as it signifies that the A site cation is too small to fill the void between the octahedra. In this paper we will concentrate on the latter type of distortion.

Due to their corner-sharing geometry, the octahedra can tilt collectively in several different patterns. By building macroscopic models of corner-shared rigid octahedra, Glazer was able to describe all 22 different patterns in which the rigid octahedra could collectively tilt and the resulting symmetry

space groups (Glazer, 1972, 1975). Later studies uncovered details about these Glazer systems through group theory and geometric considerations (Aleksandrov, 1976; O’Keeffe & Hyde, 1977; Woodward, 1997a, 1997b; Howard & Stokes, 1998).

Depending on the Glazer tilt pattern of a perovskite, the structure will have a different symmetry space group (Aleksandrov, 1976; O’Keeffe & Hyde, 1977; Woodward, 1997a,b; Howard & Stokes, 1998). Modelling the structures of these low-symmetry phases is therefore often achieved using the symmetry-broken crystallographic models and constraining the allowed atomic displacements to those imposed by the space group symmetries. However, in general, the symmetry space group allows for more displacive degrees of freedom than those strictly needed to describe the tilting of the octahedra. Using these models for fitting scattering data leads to structures where the octahedra are distorted in a way that cannot be represented in terms of the pure Glazer tilt patterns with rigid units even in the cases where the octahedra are not geometrically required to distort (Howard & Stokes, 1998).

Here we explore a more direct approach to modeling collective rotations using algebraic expressions that link displacements of atoms in the Glazer tilt systems. Going beyond purely symmetry constraints is surprisingly challenging. Approximate Monte Carlo approaches have been attempted (Sartbaeva *et al.*, 2006, 2007), where atoms are tethered to rigid-unit templates which do not distort, but are allowed to relax away from the vertices. It has also been shown (Campbell *et al.*, 2018) that, for small rotations, a set of linear equations on top of symmetry mode analysis (Perez-Mato *et al.*, 2010) can identify collective modes in a system of connected rigid units that do not (or hardly) distort the units. However, there is currently no straightforward way of incorporating this information into a refinement program for quantitative modeling of data in terms of this collective mode basis.

Our approach of explicitly building the geometric constraint equations without assumed symmetries has the advantage that it can be easily plugged into local structure modeling schemes such as that used in the *diffpy-CMI* (Juhás *et al.*, 2015) program. The program works in the space group $P1$ by design, allowing one to introduce structural distortions by moving atoms at will. The approach greatly reduces the number of refinable parameters in a physically meaningful way and can help to build intuition about the structure and how it is likely to distort. It also allows the user to directly test hypotheses about the rigidity of the units or the type of tilting present in a sample without the conceptual complexity of having to surf between space groups. This can give new insight that might be otherwise lost. Here we demonstrate the use of our code on the compound CaTiO_3 , the archetypal perovskite with a well-known Glazer tilt pattern $\alpha^+\beta^-\beta^-$.

The approach described here has been made possible by combining PDF methods, which can reveal local broken symmetries such as collective tilts, and the *diffpy-CMI* modeling code (Juhás *et al.*, 2015), which is designed to have the flexibility to build arbitrary mathematical constraints into

PDF refinements. Although demonstrated here using a simple and relatively plain perovskite, it can be easily extended to other perovskites, such as halides and nickelates. In the latter, the approach could be beneficial for disentangling octahedral tilting from breathing modes and other collective distortions. It can also be extended to other nearby structures such as the cuprate high-temperature superconductors, a perovskite-derived structure that also consists of corner-shared octahedra and polyhedra.

2. Glazer tilt definitions

The Glazer tilt systems, as laid out by Glazer (1972), describe the complete set of collective rotations allowed in a network of corner-shared octahedra as found in perovskites (shown in Table 1). These tilt patterns can all be described using a $2 \times 2 \times 2$ (or smaller) supercell of the cubic perovskite unit cell, and collective distortions requiring larger supercells are unlikely.

For clarity we use the naming scheme, as introduced by Glazer. An octahedron can be tilted around one, two or all three of the cartesian axes, x , y and z . The nature of each rotation is indicated by three Greek letters with superscripts, where the first letter denotes the rotation around x , the second around y and the third around z . Repeating letters (e.g. $\alpha^+\alpha^+\alpha^+$) indicate that the amplitudes around the specific axes are the same, whereas different letters (e.g. $\alpha^+\beta^+\gamma^+$) indicate that the tilts differ in amplitude around the different axes.

The superscripts can take the value 0, + or – to indicate a zero-tilt amplitude or a non-zero amplitude with tilts in adjacent layers along the tilt axis being either in-phase (+) or out-of-phase (–). For example, the tilt pattern $\alpha^0\alpha^0\gamma^+$ has no tilt around the x and y axes and a non-zero in-phase tilt around the z axis. Because of the connectivity of the octahedra at their corners, neighbouring octahedra in the plane perpendicular to the tilt axis rotate in the opposite direction to the central octahedron, leading to a doubling of the unit cell in that plane. In the example of $\alpha^0\alpha^0\gamma^+$, the unit cell is therefore doubled in the ab plane, but not along the z axis. On the other hand, an out-of-phase tilt, for example along the z axis in the pattern $\alpha^0\alpha^0\gamma^-$, will double the unit cell also along the tilt axis. Fig. 1 illustrates the difference between the in-phase and out-of-phase tilt pattern of the $\alpha^0\alpha^0\gamma^+$ and $\alpha^0\alpha^0\gamma^-$ tilt systems, as viewed down the tilt axis.

3. Approach

Here we describe the method for building constrained Glazer tilt pattern models. The code may be found at https://github.com/sandraskj/glazer_fitting.

Models are built using the *diffpy-CMI* program (Juhás *et al.*, 2015), which has powerful and flexible methods for specifying constraints between model parameters. This allows, in principle, large numbers of parameters to be expressed in terms of a much smaller number of variables from analytic or numerical expressions. We first generate the constraints as symbolic expressions relating multiple atoms' fractional coordinates.

Table 1

For each of the different Glazer tilt patterns we provide the index as assigned by Glazer (1972, 1975), the tilts given with Glazer notation and the space group symmetry of the resulting phase.

Note we have only included the tilt systems that are symmetry-nonequivalent.

Tilt system	Tilts	Space group
23	$\alpha^0\alpha^0\alpha^0$	$Pm\bar{3}m$ (No. 221)
22	$\alpha^0\alpha^0\gamma^-$	$I4/mcm$ (No. 140)
21	$\alpha^0\alpha^0\gamma^+$	$P4/mbm$ (No. 127)
20	$\alpha^0\beta^-\beta^-$	$Imma$ (No. 74)
19	$\alpha^0\beta^-\gamma^-$	$C2/m$ (No. 12)
17	$\alpha^0\beta^+\gamma^-$	$Cmcm$ (No. 63)
16	$\alpha^0\beta^+\beta^+$	$I4/mmm$ (No. 139)
14	$\alpha^-\alpha^-\alpha^-$	$R\bar{3}c$ (No. 167)
13	$\alpha^-\beta^-\beta^-$	$C2/c$ (No. 15)
12	$\alpha^-\beta^-\gamma^-$	$P1$ (No. 2)
10	$\alpha^+\beta^-\beta^-$	$Pnma$ (No. 62)
8	$\alpha^+\beta^-\gamma^-$	$P2_1/m$ (No. 11)
5	$\alpha^+\alpha^+\gamma^-$	$P4_2/nmc$ (No. 137)
3	$\alpha^+\alpha^+\alpha^+$	$Im\bar{3}$ (No. 204)
1	$\alpha^+\beta^+\gamma^+$	$Immm$ (No. 71)

These expressions are then captured into the *diffpy-CMI* constraint handling interface.

For the rotation of the octahedra, we set up the code such that the user only has to input the Glazer system number and the tilt amplitudes related to that tilt system. The rotations are then created by rotating three of the oxygens in each octahedron around the crystallographic axes (clockwise, anti-clockwise or none) according to the chosen Glazer tilt pattern and the tilt amplitudes. In performing these rotations, simple rotation matrices would not do as they would lead to different bond lengths to the two nearby B cations. To mitigate this issue, each oxygen is displaced in straight lines perpendicular to the line between two nearby B cations. The increased bond lengths to the B cations resulting from this operation are fixed when the lattice parameters are rescaled, as described below.

For all the Glazer tilt systems listed in Table 1 the constraints have been constructed such that the shortest $B-X$ distances are all kept rigid. Since, for most of the systems, there is a small coupling between the rotation modes around the three axes, these constraints will lead to a small octahedral distortion with octahedral angles deviating slightly from 90° , so the tilts are not strictly rigid. However, the tilt equations result in almost rigid octahedral tilting, where the collective modes may be described in terms of tilt angles around each axis which are the only refinable parameters for the modes when fitting to data, in addition to the cubic lattice parameter.

The collective octahedral rotations do not include A site ion structural parameters since the A atoms are not directly part of the octahedral tilting network. However, their positions are still refined, as they do indirectly respond to the octahedral tilts by displacement. We chose to constrain the A cation displacements in such a way as to respect the expected symmetry of the tilted structure, which in the case of CaTiO_3 is the space group $Pnma$.

Activating tilt modes leads to well-defined reductions in the lattice parameters, and therefore for a full description, we need to find the appropriate scaling parameters expressed in

terms of the Glazer tilt amplitudes and the lattice parameter of the cubic parent structure. We start with the interatomic vectors from the B atom at the origin to its three unique X neighbors in the octahedron, \mathbf{r}_{B-X_1} , \mathbf{r}_{B-X_2} and \mathbf{r}_{B-X_3} ,

$$|\mathbf{r}_{B-X_1}| = \left[(a'/4)^2 + (b'y_{X_1})^2 + (c'z_{X_1})^2 \right]^{1/2}, \quad (2)$$

$$|\mathbf{r}_{B-X_2}| = \left[(a'x_{X_2})^2 + (b'/4)^2 + (c'z_{X_2})^2 \right]^{1/2}, \quad (3)$$

$$|\mathbf{r}_{B-X_3}| = \left[(a'x_{X_3})^2 + (b'y_{X_3})^2 + (c'/4)^2 \right]^{1/2}, \quad (4)$$

where a' , b' and c' are the lattice parameters of the distorted supercell for a given set of Glazer tilts. Keep in mind that the fractional coordinates y_{X_1} , z_{X_2} etc. are all expressions containing the Glazer tilt variables and the lattice parameter of the cubic parent structure a_h . Next, we set each of the bond lengths to be a quarter of the parent unit cell a_h ,

$$|\mathbf{r}_{B-X_1}| = |\mathbf{r}_{B-X_2}| = |\mathbf{r}_{B-X_3}| = a_h/4. \quad (5)$$

Since the rotations are assumed to be those of rigid octahedra, these lengths will not change after the rotation. This allows us to relate the lattice parameters of the Glazer tilt distorted supercell to those of the cubic parent cell through scaling parameters s_a , s_b and s_c ,

$$a' = \frac{2a_h}{s_a}, b' = \frac{2a_h}{s_b}, c' = \frac{2a_h}{s_c}. \quad (6)$$

Substituting for a' , b' and c' in Equations (2)–(4), we get a set of three equations,

$$|\mathbf{r}_{B-X_1}| = \left[\frac{1}{4s_a^2} + \left(\frac{2y_{X_1}}{s_b} \right)^2 + \left(\frac{2z_{X_1}}{s_c} \right)^2 \right]^{1/2} = \frac{1}{4}, \quad (7)$$

$$|\mathbf{r}_{B-X_2}| = \left[\left(\frac{2x_{X_2}}{s_a} \right)^2 + \frac{1}{4s_b^2} + \left(\frac{2z_{X_2}}{s_c} \right)^2 \right]^{1/2} = \frac{1}{4}, \quad (8)$$

$$|\mathbf{r}_{B-X_3}| = \left[\left(\frac{2x_{X_3}}{s_a} \right)^2 + \left(\frac{2y_{X_3}}{s_b} \right)^2 + \frac{1}{4s_c^2} \right]^{1/2} = \frac{1}{4}, \quad (9)$$

that can be solved for s_a , s_b and s_c ,

$$s_a = \left\{ \frac{1 - 256x_{X_2}^2(y_{X_1}^2 - 16y_{X_3}^2z_{X_1}^2) - 256[y_{X_3}^2z_{X_2}^2 + x_{X_3}^2(z_{X_1}^2 - 16y_{X_1}^2z_{X_2}^2)]}{1 - 16y_{X_1}^2 + 16(-1 + 16y_{X_3}^2)z_{X_1}^2 + 256(y_{X_1}^2 - y_{X_3}^2)z_{X_2}^2} \right\}^{1/2}, \quad (10)$$

$$s_b = \left\{ \frac{1 - 256x_{X_2}^2(y_{X_1}^2 - 16y_{X_3}^2z_{X_1}^2) - 256[y_{X_3}^2z_{X_2}^2 + x_{X_3}^2(z_{X_1}^2 - 16y_{X_1}^2z_{X_2}^2)]}{1 + 16x_{X_2}^2(-1 + 16z_{X_1}^2) - 16z_{X_2}^2 + 256x_{X_3}^2(-z_{X_1}^2 + z_{X_2}^2)} \right\}^{1/2}, \quad (11)$$

$$s_c = \left\{ \frac{-1 - 256x_{X_2}^2(y_{X_1}^2 - 16y_{X_3}^2z_{X_1}^2) + 256[y_{X_3}^2z_{X_2}^2 + x_{X_3}^2(z_{X_1}^2 + 16y_{X_1}^2z_{X_2}^2)]}{-1 + x_{X_3}^2(16 - 256y_{X_1}^2) + 256x_{X_2}^2(y_{X_1}^2 - y_{X_3}^2) + 16y_{X_3}^2} \right\}^{1/2}, \quad (12)$$

Setting these as constraints in the refinement allows the unit cell to change size according to the tilt amplitude without introducing any extra refinable parameters.

We present the full constraints for Glazer system 10, as generated from the code, in the project code repository on GitHub (https://github.com/sandraskj/glazer_fitting). In the GitHub repository we also provide the code that generates the constraints for all the Glazer systems and brief instructions for how the reader can download them and how to set it up for their own refinements using *diffpy-CMI*.

4. Experimental measurements

To obtain experimental pair distribution functions (PDFs) for CaTiO_3 , total scattering measurements were carried out at the 28-ID-1 (PDF) beamline at the NSLS-II at Brookhaven National Laboratory on a commercially purchased powder sample of CaTiO_3 (Strem Chemicals Inc. CAS 12049-50-2). A 2D Perkin Elmer amorphous silicon detector was placed 380 mm behind the sample, which was loaded in a 0.5 mm glass capillary. The wavelength of the incident X-rays was 0.16635 Å. Data were collected at 200 K for 60 s in a flowing nitrogen cryostream.

The data were processed using standard methods (Egami & Billinge, 2012). The instrument geometry was calibrated using data from a fine Ni powder using *pyFAI* (Kieffer *et al.*, 2020). 2D diffraction patterns were processed by applying masks to remove the beam stop as well as outlier-saturated and dead pixels using a home-written automasking protocol. After correction for polarization effects, intensities were integrated azimuthally along circles of constant scattering vector magnitude, Q , also using *pyFAI*. The background signal from an empty glass capillary was subtracted and the data were normalized and corrected to obtain the reduced total scattering structure function, $F(Q)$, which was Fourier transformed to obtain the PDF. This was achieved using *PDFgetX3* (Juhás *et al.*, 2013). The maximum range of data used in the Fourier transform was $Q_{\text{max}} = 23.6 \text{ \AA}^{-1}$.

For both the measured and the simulated PDFs we use the correlation function $G(r)$ (PDF), based on its close relation to the experimental data as it is the Fourier transform of the scattering function with no external information such as density, and also because it has a constant uncertainty in r (Keen, 2001; Egami & Billinge, 2012).

Modelling the experimental PDF data was carried out using both the space group *Pnma* and the Glazer model. The *Pnma* model is a $\sqrt{2} \times \sqrt{2} \times 2$ supercell of the cubic aristotype, while the Glazer model is a $2 \times 2 \times 2$ supercell (all our Glazer models use a $2 \times 2 \times 2$ supercell basis regardless of the final symmetry). Isotropic U_{iso} values were defined for each element, giving three variables $U_{\text{iso}}(\text{Ca})$, $U_{\text{iso}}(\text{Ti})$ and $U_{\text{iso}}(\text{O})$.

5. Results

Our initial robustness tests of the approach are carried out on simulated PDF data of CaTiO_3 with a well-defined tilt pattern according to the known ground-state structure.

The structure was created in Glazer system No. 10 with an in-phase tilt around one axis of $\alpha = 9^\circ$ and out-of-phase tilt around the other two axes of $\beta = 10^\circ$. For simplicity, in the constructed structure there was no displacement of the Ca atoms from their cubic positions. The isotropic atomic displacement parameters for all the ions were set to $U_{\text{iso}}(\text{Ca}) = 0.0030 \text{ \AA}^2$, $U_{\text{iso}}(\text{Ti}) = 0.0046 \text{ \AA}^2$ and $U_{\text{iso}}(\text{O}) = 0.011 \text{ \AA}^2$, similar to those obtained from fitting an experimentally measured PDF of CaTiO_3 with a conventional $Pnma$ model between 1.6 and 50 \AA (discussed below), as shown in Table 2.

The PDF was simulated from the structure using *diffpy-CMI* (Juhás *et al.*, 2015), with damping and broadening parameters set to the values 0.029 \AA^{-1} and 0.010 \AA^{-1} , respectively, obtained from the calibration sample in our measurement and $Q_{\text{max}} = 23.6 \text{ \AA}^{-1}$, the same value we used for the experimental data.

We then fit constrained Glazer models from each of the 22 Glazer tilt patterns to the data from $1.6 < r < 15 \text{ \AA}$. The starting values for the tilt amplitudes in the refinement models were set to values that were roughly 70% of the true values in the structure for the simulated dataset.

The fits with the one-tilt and two-tilt models were poor in most cases, whereas all three-tilt systems gave fit residuals below 10%. Tilt system 10 (the ground-truth result) is one of the three-tilt systems so this gives confidence that the approach can easily differentiate the presence or absence of tilts. However, within the subset of three-tilt systems, different families of tilt combinations can be found which refine to significantly different R_w values, as shown in Fig. 2. Interestingly, the fits can differentiate cases that have $+++$, $++-$, $+--$ and $---$ tilts, but within those families it can only weakly distinguish between different Glazer systems. This may be because the tilt amplitudes we chose for the test, coming from the observed values in CaTiO_3 , are close to each other.

The best overall fit was found for Glazer system 10, the correct one, as well as Glazer system 8 that has qualitatively the same tilt pattern but with an extra degree of freedom that allows the two out-of-phase tilts to be of different amplitudes. This shows that the collective mode refinements are working in *diffpy-CMI*.

Next, we performed refinements on an experimental dataset of CaTiO_3 . We performed the refinements with two models: one using our formulation based on Glazer tilt system 10 and, for comparison, a model with constraints consistent with the crystallographic space group $Pnma$, which allows tilt distortions but does not impose the constraint of those tilts to be rigid. The Ca sites were constrained the same way in both models, according to the space-group symmetry of $Pnma$. The space-group model has ten structural degrees of freedom, whereas the Glazer model has only five. The variables, including explicitly refined as well as post-calculated ones, and their values after refinement over 1.6–50 \AA are listed in Table 2.

Table 2

Comparison of parameters from the space-group and Glazer model refinements over the r range 1.6–50 \AA .

Two values are given each for α and β in the space-group model because different octahedra tilt by different amounts. We note that the space-group model $Pnma$ is a $\sqrt{2} \times \sqrt{2} \times 2$ supercell of the cubic aristotype while the Glazer model is a $2 \times 2 \times 2$ supercell. To aid comparison of the values, we converted the lattice parameters of the Glazer model to a $\sqrt{2} \times \sqrt{2} \times 2$ basis. delta1 accounts for correlated atomic motion effects that sharpen the nearest neighbor PDF peak (Egami & Billinge, 2012).

Pnma space-group model		Glazer model	
Variable	Value	Variable	Value
Scale	0.18	Scale	0.17
delta1	1.03	delta1	2.47
a	5.428	a_h	3.907
b	7.620	a^\dagger	5.402
c	5.366	b^\dagger	7.594
x_{Ca}	0.0357	c^\dagger	5.402
z_{Ca}	0.0031	x_{Ca}	0.0216
α^\dagger ($^\circ$)	9.6, 10.1	y_{Ca}	0.0069
β^\dagger ($^\circ$)	7.1, 10.6	α ($^\circ$)	7.6
x_{O1}	0.2059	β ($^\circ$)	9.7
y_{O1}	0.0335		
z_{O1}	0.2073		
x_{O2}	0.0155		
z_{O2}	0.5784		
$U_{\text{iso}}(\text{Ca})$	0.005	$U_{\text{iso}}(\text{Ca})$	0.004
$U_{\text{iso}}(\text{Ti})$	0.003	$U_{\text{iso}}(\text{Ti})$	0.004
$U_{\text{iso}}(\text{O})$	0.010	$U_{\text{iso}}(\text{O})$	0.011
R_w	0.087	R_w	0.245

\dagger Parameters were not explicit variables of the respective models, and their values were calculated post-refinement using the optimized atomic positions of the structure.

Fitting both models over this wide- r range (Fig. 3), we can see that the space-group model provides a significantly smaller fit residual (space group gives $R_w = 0.087$ while the Glazer model gives $R_w = 0.245$), which is not surprising given its larger number of refinable variables. Comparing the refined structural parameters from the two models, we see that all except for the tilt angles and the lattice parameters are in quite good agreement, as shown by comparing the values in Table 2.

The information of interest to us is the presence and amplitude of rigid Glazer tilt modes. For the Glazer model these are a direct output of the program. For comparison, we

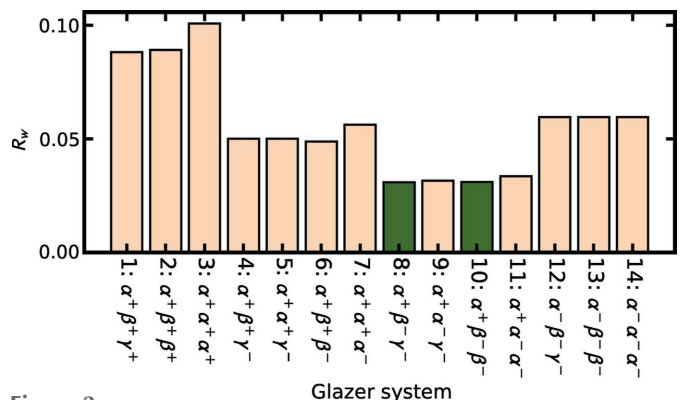


Figure 2

Comparison of the fit of the 14 three-tilt Glazer systems to a simulated PDF of CaTiO_3 with octahedral rotations but without Ca displacements.

also calculate the tilt angles from the space group by finding the angle that each vector between opposite pairs of oxygen atoms on an octahedron makes with the pseudocubic axes. This gives two values for each of the tilt angles due to octahedral distortion, in contrast with previous studies that only reported one value for each (Kennedy *et al.*, 1999; Yashima & Ali, 2009). Our choice to present both values obtained for each tilt angle highlights the difference in rigidity and robustness of the space-group and Glazer-mode constrained models.

The Glazer model results in values of in-phase tilt $\alpha = 7.6^\circ$ and out-of-phase tilt $\beta = 9.7^\circ$. The space-group model gives the values $\alpha = 9.6$ and 10.1° and $\beta = 7.1$ and 10.6° . The average value of the in-phase α tilt is higher in the space-group model by almost 2° than in the Glazer model, and that of the out-of-phase β tilt is lower by about 1° . In the case of β the two different octahedra in the space-group model are quite different and actually straddle the value obtained in the Glazer fit.

Addressing the difference in fit quality, we believe that a significant contribution to the poorer fit can be attributed to the tighter constraints on the lattice parameters in the Glazer fits. The space-group model is orthorhombic, with three different lattice parameters. For the Glazer model, the shape of the unit cell changes in strict accordance with the chosen tilt pattern, and only one lattice parameter variable (the initial cubic lattice parameter) is refined. We note that, for the particular tilt pattern $\alpha^+\beta^-\beta^-$ the unit cell is tetragonal, not orthorhombic (Table 2). The $a = c$ parameters for the Glazer model lie between those of the space-group model, but are not able to separate into short and long values allowed by the orthorhombic crystallographic model due to the Glazer model

constraints, whereas clearly structural relaxations beyond the rigid tilts are present in the actual material.

If the difference in R_w between the two models in the wide-range fits is due to the difference in model rigidity, the models would be expected to perform more comparably when fitting only the most local structure, and for the Glazer model to perform worse at higher values of r . The Glazer model only allows for the degrees of freedom that are strictly necessary for the tilt pattern $\alpha^+\beta^-\beta^-$, and comparing the two fits at different length scales therefore allows us to separate contributions to the PDF signal that come from rigid tilts and additional non-rigid relaxations. It is also interesting to consider if the refined values of the Glazer tilts vary with the r range that is fit over, as might be the case if the tilts become damped with increasing r . We therefore performed a series of fits where an r range of a fixed size (referred to as a box) is shifted incrementally up to higher values, an approach we call a ‘boxcar’ fit. The r -dependence of the refined variables are shown in Fig. 4.

As evident in Figs. 4(b) and 4(c) the values of the tilt amplitudes vary more smoothly in the Glazer model than in the space-group model indicating that refinement of these variables is more stable in the more highly constrained Glazer fits. Also, whilst the α tilt is fairly r -independent, there is a marked tendency for the β tilt to decrease with increasing r in the Glazer fit. We also see a similar trend in the total displacement of Ca from cubic positions [δ_{Ca} , Fig. 4(d)], with the Glazer model trending downwards, while the space-group model stays at the same value throughout the r range. One possible explanation for the downwards trends of these structural parameters is a loss of structural coherence with increasing r due to a non-rigidity, for example in cases where local tilts survive in a material but are not present globally. The range of coherence of the collective motions may then be measured by this approach. Another explanation is that the unit-cell shape of the model is too constrained to adequately describe even the local structure, a constraint that is exacerbated at higher r . To check which of these two scenarios is the case for CaTiO_3 , we also performed boxcar fits on a simulated PDF of CaTiO_3 . We constructed two versions of the structure, both with well defined tilts of $\alpha = 9^\circ$ and $\beta = 10^\circ$ and A site displacements similar to those found for the space group fit in Table 2, but one in which the lattice parameters were constrained by the tilt pattern (tetragonal cell) and one with orthorhombic lattice parameters similar to the known ground-state structure. The results, provided in the supporting information, show that both the Glazer and space-group models perform similarly over the entire r range for the simulated PDF of the tetragonal, ‘pure’ Glazer tilted structure, whereas the fits of the PDF of the orthorhombic structure give trends in R_w that strongly match the data in Fig. 4(a). It is therefore reasonable to conclude that the imposed tetragonality of the Glazer model does not adequately allow for the orthorhombicity in the measured CaTiO_3 . Presumably other structural degrees of freedom in the structure such as A site displacements cause the global unit cell to relax from tetragonal to orthorhombic, though this is not imposed by the tilts.

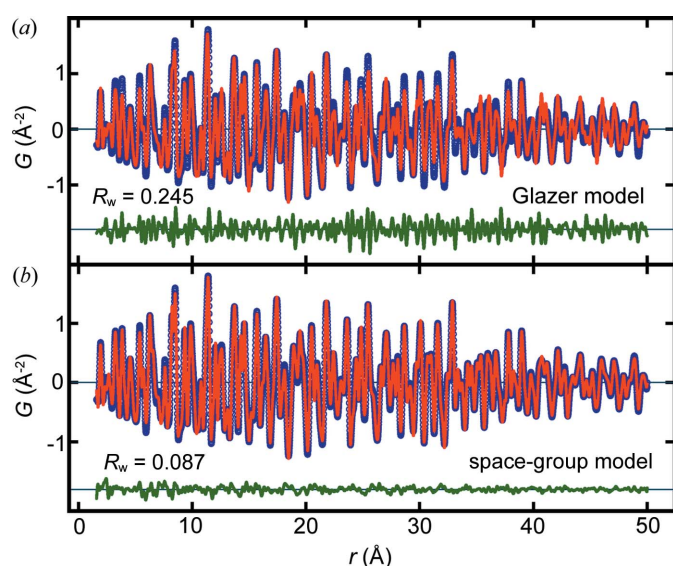
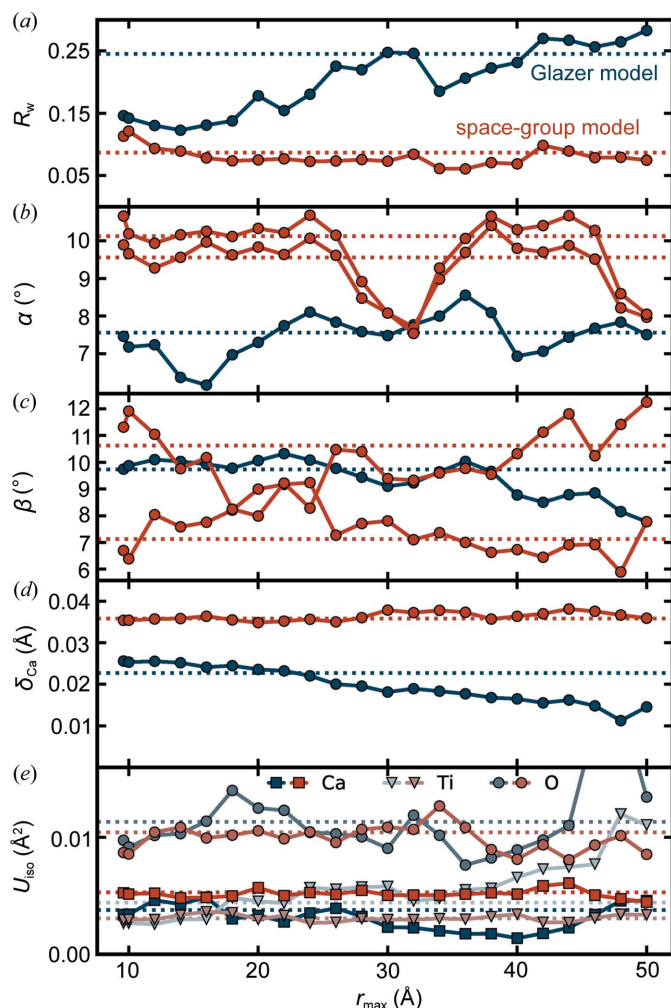


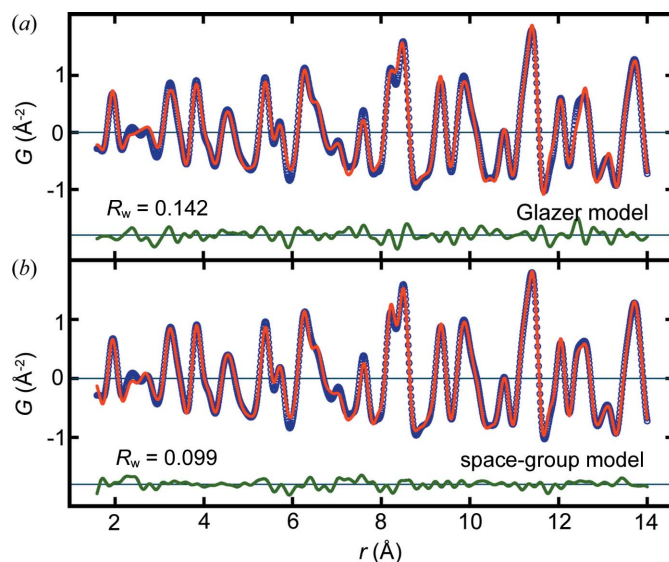
Figure 3 Plots of measured (blue) and best-fit (red) PDFs of CaTiO_3 with the difference curve plotted in green offset below over the r range 1.6–50 \AA . The model for the best-fit PDF is from (a) the constrained Glazer tilt model in Glazer system 10 and (b) allowing all the structural degrees of freedom of the $Pnma$ space-group model.


Figure 4

Comparison of the (a) fit residual R_w , the octahedral tilt amplitudes (b) α and (c) β , (d) the total Ca displacements (δ_{Ca}), and (e) the U_{iso} values from boxcar fits with the space-group model and the Glazer model of $CaTiO_3$ at 200 K. The r range (or ‘the box’) was set to 8 Å and incrementally shifted to higher r values in steps of 2 Å. The labels on the x axis correspond to the highest value in the box, r_{max} . The dotted lines represent the values obtained from a fit over the 1.6–50 Å range. We note that, for the space-group model, the tilt angles α and β differ depending on which octahedra were used to calculate them, and such are represented by two different lines.

As the tetragonal constraint of the Glazer model is expected to be exacerbated with increasing r , we expect a good agreement between the Glazer and space-group models at low r . A comparison for the fits over the range $r = 1.6$ –14 Å is shown on an expanded scale in Fig. 5, where the R_w values are indeed comparable.

We note that for the case we studied, $CaTiO_3$ at room temperature, the tilts are long-range ordered and so are expected to persist over large distances, asymptotically approaching the crystallographic values. This kind of boxcar analysis can be expected to be more interesting in materials where no tilts are observed in the average structure but are observed locally (Skjærvø *et al.*, 2019; Bozin *et al.*, 2019; Koch *et al.*, 2021; Yang *et al.*, 2020; Wang *et al.*, 2020; Senn *et al.*, 2016). Expanding the Glazer model to accommodate changes in unit-cell shape beyond that predicted by the tilt pattern


Figure 5

Plots of measured (blue) and best-fit (red) PDFs of $CaTiO_3$ with the difference curve plotted in green offset below over the r range 1.6–14 Å. The model for the best-fit PDF is from (a) the constrained Glazer tilt model in Glazer system 10 and (b) allowing all the structural degrees of freedom of the $Pnma$ space-group model.

would allow us to keep the benefits of a highly constrained model while mitigating poorer fits at high r due to too strict lattice parameters and therefore allow us to explore any potential effects of loss of coherence on the fit residual.

6. Conclusions

We have developed sets of constraint equations that explicitly model octahedral tilts (Glazer tilts) in perovskites. The model allows refinements of collective atomic motions by geometrically connecting atoms in the lattice, allowing rigid rotations to be modeled directly. We have implemented the constraints directly in the PDF modeling program *diffpy-CMI*.

We have demonstrated the use of our code on the canonical tilted perovskite system $CaTiO_3$, which has a known long-range ordered Glazer tilt system $\alpha^+\beta^-\beta^-$. We found that our Glazer model fits comparably to the known space-group model $Pnma$ below $r = 14$ Å. We further observed that the Glazer model performed progressively worse at higher r due to the rigidity of the model. In this case the rigid tilts alone broke the cubic symmetry to tetragonal, whereas the observed symmetry is orthorhombic, which explains the discrepancy in the fit residuals. Presumably, non-rigid relaxations and relaxations of atoms not involved in the tilts are responsible for the additional reduction in symmetry.

Our Glazer model could be used to study a wide range of perovskite systems to better understand whether their structure is well explained in terms of pure octahedral rotations, how the rotations vary with parameters such as temperature and pressure, and what additional structural relaxations are needed to explain the structure beyond the simple picture of octahedral rotations. The highly constrained fits can be expected to give stable refinements even when data quality is

limited, for example, from small nanoparticles or powders in a diamond anvil cell. The work also highlights the strengths and limitations of the geometric approach in building rigid-body constraints.

Acknowledgements

We acknowledge Daniel E. DeRosha and Jonathan Owen for help in preparing the CaTiO₃ sample, and Milinda Abeykoon and Gihan Kwon for their help with collecting data at the 28-ID-1 (PDF) beamline at the NSLS-II.

Funding information

This work was supported by the US National Science Foundation, Directorate for Mathematical and Physical Sciences (grant No. DMREF-1922234 awarded to SJLB and SHS). MAK acknowledges support from the Carlsberg Foundation (grant no. CF17-0823). Use of the National Synchrotron Light Source II, Brookhaven National Laboratory, was supported by the US Department of Energy, Office of Science, Office of Basic Energy Sciences (contract No. DE-SC0012704).

References

- Aleksandrov, K. S. (1976). *Ferroelectrics*, **14**, 801–805.
- Benedek, N. A. & Fennie, C. J. (2013). *J. Phys. Chem. C*, **117**, 13339–13349.
- Bhalla, A., Guo, R. & Roy, R. (2000). *Mater. Res. Innovations*, **4**, 3–26.
- Bozin, E. S., Yin, W. G., Koch, R. J., Abeykoon, M., Hor, Y. S., Zheng, H., Lei, H. C., Petrovic, C., Mitchell, J. F. & Billinge, S. J. L. (2019). *Nat. Commun.* **10**, 3638.
- Campbell, B. J., Averett, T., Yost, C., Machlus, S., Stokes, H. T., Whittle, T. A., Schmid, S. & Howard, C. J. (2018). *Acta Cryst.* **A74**, a286–a286.
- Dove, M. T. (1997). *Am. Mineral.* **82**, 213–244.
- Egami, T. & Billinge, S. J. L. (2012). *Underneath the Bragg Peaks: Structural Analysis of Complex Materials*, 2nd ed. Amsterdam: Elsevier.
- Glazer, A. M. (1972). *Acta Cryst.* **B28**, 3384–3392.
- Glazer, A. M. (1975). *Acta Cryst.* **A31**, 756–762.
- Goldschmidt, V. M. (1926). *Naturwissenschaften*, **14**, 477–485.
- Goodenough, J. B. (1955). *Phys. Rev.* **100**, 564–573.
- Howard, C. J. & Stokes, H. T. (1998). *Acta Cryst.* **B54**, 782–789.
- Juhás, P., Davis, T., Farrow, C. L. & Billinge, S. J. L. (2013). *J. Appl. Cryst.* **46**, 560–566.
- Juhás, P., Farrow, C., Yang, X., Knox, K. & Billinge, S. (2015). *Acta Cryst.* **A71**, 562–568.
- Keen, D. A. (2001). *J. Appl. Cryst.* **34**, 172–177.
- Kennedy, B. J., Howard, C. J. & Chakoumakos, B. C. (1999). *J. Phys. Condens. Matter*, **11**, 1479–1488.
- Kieffer, J., Valls, V., Blanc, N. & Hennig, C. (2020). *J. Synchrotron Rad.* **27**, 558–566.
- Koch, R. J., Sinclair, R., McDonnell, M. T., Yu, R., Abeykoon, M., Tucker, M. G., Tselik, A. M., Billinge, S. J. L., Zhou, H. D., Yin, W.-G. & Bozin, E. S. (2021). *Phys. Rev. Lett.* **126**, 186402.
- Kwei, G. H., Billinge, S. L., Cheong, S.-W. & Saxton, J. G. (1995). *Ferroelectrics*, **164**, 57–73.
- Kwei, G. H., Lawson, A. C., Billinge, S. J. L. & Cheong, S. W. (1993). *J. Phys. Chem.* **97**, 2368–2377.
- Müller, K. A., Berlinger, W. & Waldner, F. (1968). *Phys. Rev. Lett.* **21**, 814–817.
- O’Keeffe, M. & Hyde, B. G. (1977). *Acta Cryst.* **B33**, 3802–3813.
- Paillard, C., Bai, X., Infante, I. C., Guennou, M., Geneste, G., Alexe, M., Kreisel, J. & Dkhil, B. (2016). *Adv. Mater.* **28**, 5153–5168.
- Perez-Mato, J. M., Orobengoa, D. & Aroyo, M. I. (2010). *Acta Cryst.* **A66**, 558–590.
- Salje, E. (1990). *Ferroelectrics*, **104**, 111–120.
- Sartbaeva, A., Wells, S. A., Thorpe, M. F., Božin, E. S. & Billinge, S. J. L. (2007). *Phys. Rev. Lett.* **99**, 155503.
- Sartbaeva, A., Wells, S. A., Thorpe, M. F. E. S., Božin, E. S. & Billinge, S. J. L. (2006). *Phys. Rev. Lett.* **97**, 065501.
- Senn, M. S., Keen, D. A., Lucas, T. C. A., Hriljac, J. A. & Goodwin, A. L. (2016). *Phys. Rev. Lett.* **116**, 207602.
- Skjærø, S. H., Meier, Q. N., Feygenson, M., Spaldin, N. A., Billinge, S. J. L., Bozin, E. S. & Selbach, S. M. (2019). *Phys. Rev. X*, **9**, 031001.
- Wang, Z., Zhao, X.-G., Koch, R., Billinge, S. J. L. & Zunger, A. (2020). *Phys. Rev. B*, **102**, 235121.
- Woodward, P. M. (1997a). *Acta Cryst.* **B53**, 32–43.
- Woodward, P. M. (1997b). *Acta Cryst.* **B53**, 44–66.
- Yang, L., Koch, R. J., Zheng, H., Mitchell, J. F., Yin, W., Tucker, M. G., Billinge, S. J. L. & Bozin, E. S. (2020). *Phys. Rev. B*, **102**, 235128.
- Yashima, M. & Ali, R. (2009). *Solid State Ionics*, **180**, 120–126.